**Classification:** Physical Sciences: Chemistry; Biological Sciences: Medical Sciences

# Mucinase-engineered cell membrane nanovesicles degrade the glycocalyx shield to potentiate antitumor immunity

Running title: Breaking the glycocalyx shield with nanoengineered mucinase for cancer immunotherapy

Xiaorui Geng[a,1], Silan Liu[a,b,c,1], Yuanwei Pan[a], Yun Ge[a,b,d,2], and Lang Rao[a,b,2]

[a] Institute of Chemical Biology, Shenzhen Bay Laboratory, Shenzhen 518132, China.

[b] Shenzhen Medical Academy of Research and Translation, Shenzhen 518107, China.

[c] Westlake University, Hangzhou 310030, China.

[d] State Key Laboratory of Chemical Oncogenomics, School of Chemical Biology and Biotechnology, Peking University Shenzhen Graduate School, Shenzhen 518055, China.

[1] X.G. and S.L. contributed equally to this work.

[2] Corresponding e-mails: geyun@szbl.ac.cn (Y.G.); lrao@szbl.ac.cn (L.R.).

## Abstract

The tumor glycocalyx forms a protective shield that masks checkpoint proteins and compromises the efficacy of immunotherapies. While the bacterial protease StcE can degrade this barrier by cleaving O-glycosylated mucin domains, its therapeutic potential is hindered by off-target toxicity and high immunogenicity. To overcome these limitations, we developed a biomimetic platform of cell membrane fusion nanovesicles (FNVs) that co-display StcE and CD47 nanobodies (nCD47) for spatially controlled glycocalyx degradation and enhanced checkpoint blockade. Using the SpyTag/SpyCatcher system, we generated StcE-displaying NVs, which were then fused with nCD47-displaying NVs. The resulting StcE-nCD47-FNVs retained potent mucin-hydrolyzing activity and exhibited well-defined physicochemical properties. By removing the mucin barrier, StcE-nCD47-FNVs significantly enhanced nCD47 binding to CD47 on tumor cells, thereby potentiating antitumor immune responses. More importantly, benefiting from prolonged circulation of FNVs and tumor targeting of nCD47, the StcE-nCD47-FNVs platform demonstrated superior tumor accumulation and biosafety compared to free StcE. In murine models of colorectal and breast cancer, StcE-nCD47-FNVs significantly suppressed tumor growth and metastasis by remodeling the tumor microenvironment, as evidenced by increased M1 macrophage polarization and CD8$^+$ T cell infiltration. By integrating glycocalyx engineering with vesicle nanotechnology, StcE-nCD47-FNVs offer a safe, robust, and versatile strategy to breach the tumor glycocalyx for next-generation cancer immunotherapy.

**Keywords:** Glycoengineering, Nanobiotechnology, Cellular vesicles, Drug delivery, Cancer immunotherapy.

## Significance Statement

The tumor glycocalyx limits antibody access to surface receptors, underscoring the need for strategies that degrade this barrier to enhance checkpoint blockade therapy. This study pioneers a tumor-targeted glycocalyx-degrading platform that synergizes mucinase activity with checkpoint blockade to overcome therapeutic resistance. By engineering fusion nanovesicles co-displaying bacterial protease StcE and CD47 nanobodies, the resulting StcE-nCD47-FNVs platform achieves localized glycocalyx removal while enhancing CD47-SIRPα axis blockade, thus boosting macrophage phagocytosis and cytotoxic T cell infiltration. Benefiting from superior tumor accumulation and biosafety, this strategy significantly suppresses tumor growth and metastasis in colorectal and breast cancer models. By combining glycocalyx engineering with checkpoint blockade, this work offers a blueprint for next-generation immunotherapies against physical and molecular barriers in solid and metastatic tumors.

## Introduction

Immune checkpoint blockade (ICB) therapy activates antitumor immune responses by using antibodies to block immune checkpoints (1, 2). Among these, the CD47-SIRPα axis has attracted interest for its role in suppressing macrophage phagocytosis (3). Although monoclonal antibodies targeting CD47-SIRPα, such as Magrolimab and Lemzoparlimab (4), have shown encouraging preclinical results, they still exhibit limited effectiveness in clinical trials (5). The glycocalyx on the surface of tumor cells act as a potential obstacle for ICB therapy (6). In tumors such as breast and colorectal cancers, aberrant overexpression and glycosylation of mucins (*e.g.*, MUC1, MUC2, and MUC5AC) result in the formation of a glycocalyx layer hundreds of nanometers thick (7, 8). These dimensions far exceed the heights of therapeutic targets such as HER2 (~15 nm) (9), PD-L1 (~7 nm) (10) and CD47 (~10 nm) (11), thereby impeding the binding of drugs. Therefore, developing strategies to effectively degrade the mucin-rich glycocalyx is critical for enhancing ICB therapy.

Current strategies targeting the glycocalyx mainly focus on inhibiting mucin synthesis or glycosylation (12). However, these approaches cannot effectively remove the pre-existing glycocalyx. In contrast, direct enzymatic degradation represents a more efficient solution (13). Among the potential enzymatic candidates, the secreted protease of C1-esterase inhibitor (StcE) from *Escherichia coli* can precisely cleave heavily O-glycosylated mucin domains, thereby efficiently removing the glycocalyx from cell surfaces (14). Despite its potential, the broad application of StcE is limited by considerable safety concerns. On one hand, because the glycocalyx is widely expressed in normal tissues, systemic administration of StcE may cause non-specific tissue damage (15). On the other hand, as a bacterial-derived heterologous protease, systemic administration of StcE may raise additional biosafety concerns (16). Therefore, improving the biocompatibility and tumor targeting of StcE is critical for its effective integration into ICB therapy.

Many functional proteins are intercellularly transported *via* extracellular vesicles (EVs) secreted by cells through budding or endosomal pathways (17). These EVs possess inherent homotypic targeting, low immunogenicity, and prolonged circulation, making them attractive delivery platforms, but their low production efficiency limits practical applications (18). Accordingly, engineered cell-derived nanovesicles (NVs) are prepared by isolating cellular membranes *via* differential centrifugation, dispersing the membrane fragments by ultrasonication to allow self-assembly, and extruding through membranes to obtain uniform vesicles (19). This process increases yield by about 50 to 100-fold while largely preserving the biological properties of EVs, providing an efficient platform to enhance StcE biocompatibility and reduce off-target toxicity (20, 21). Moreover, the engineerability of NVs offers distinct advantages over traditional antibody-enzyme conjugation methods, which often suffer from loss of enzymatic activity due to random chemical coupling or inefficient expression of large fusion proteins (22, 23). In particular, NVs enable the co-display of StcE and nCD47 through precise engineering. Our previous work demonstrated the successful surface display of nCD47 on NVs (24), whereas direct genetic fusion of large proteins such as StcE remains challenging. To overcome this limitation, the SpyTag-SpyCatcher system can be employed to achieve controllable, topology-specific covalent conjugation while preserving enzymatic activity (25, 26). Therefore, NVs provide an efficient platform to safely and controllably degrade the glycocalyx, enabling synergistic integration with ICB therapy.

Herein, we report the development of engineered fusion NVs as a versatile platform co-displaying StcE and nCD47 *via* the SpyTag-SpyCatcher system. The resulting StcE-nCD47-FNVs effectively degraded the glycocalyx, exposing the masked CD47 epitopes on tumor cells and enhancing the blockade of the CD47-SIRPα axis. Moreover, co-display of nCD47 imparted StcE-nCD47-FNVs to anchor to the tumor surface post-degradation of mucin, establishing a positive feedback loop that concentrates the hydrolytic activity of StcE at the tumor site to mitigate non-specific toxicity. In both colorectal cancer and breast cancer lung metastasis models, treatment with StcE-nCD47-FNVs remodeled the tumor microenvironment by enhancing the infiltration of M1 macrophages and CD8$^+$ T cells. This synergistic integration of targeted glycocalyx degradation with ICB, translated into enhanced efficacy in suppressing tumor growth and metastasis.

## Results

### Display of StcE on cell surfaces *via* a bioconjugation strategy

The dense glycocalyx on the tumor cell surface presents a physical barrier that sterically hinders the binding of therapeutic agents, such as nCD47, to immune checkpoints like CD47 (27). To overcome this, we developed NVs-based system utilizing the mucin-specific protease StcE, hypothesizing that targeted degradation of the glycocalyx would unmask these underlying epitopes (Fig. 1*A*). In this work, the structure of StcE deleted the C-terminal X409 domain for reduced nonspecific binding (Fig.

S1). Firstly, StcE and its inactive mutant (StcE E447D, lacking enzymatic activity, hereafter denoted as StcE*), were expressed and purified as previously reported (Fig. S2*A*) (28). The enzymatic activity of StcE was verified by cleavage of the recombinant C1 esterase inhibitor (C1INH) substrate (Fig. S2*B*) and reduction of MUC1 levels on HeLa cells (Fig. S3). Moreover, AF647-labeled StcE* was validated as an effective mucin probe, exhibiting a staining pattern comparable to commercial anti-MUC1 antibodies (Fig. S3*C*). Staining with AF647-StcE* revealed that various mouse tumor cell lines, including 4T1, CT26, and B16F10, expressed surface mucins that were highly susceptible to StcE-mediated degradation (Fig. 1*B*-*C*). These findings demonstrated that StcE could effectively remove the mucin on various cancer cells.

Given that NVs function as biocompatible carriers for surface enzyme presentation (29), we first aimed to display StcE on HEK293T cells. Direct membrane display of HA-tagged StcE or StcE* on HEK293T cells via lentiviral transduction failed to yield detectable expression, likely due to the high molecular weight and potential toxicity of StcE (Fig. S4). Therefore, an indirect bioconjugation strategy was adopted using the SpyTag003 (ST)-SpyCatcher003 (SC) system, which spontaneously forms a covalent isopeptide bond (30). HEK293T cells were engineered to express SC (HEK293T-SC) for covalent conjugation of StcE bearing ST (StcE-ST) (Fig. 1*D*). Cleavage assays confirmed that StcE-ST retained enzymatic activity comparable to StcE against both C1INH and mucins on HeLa cells (Fig. S2*B*, S5). SDS-PAGE demonstrated efficient *in vitro* conjugation of StcE-ST and SC (Fig. S6). Robust surface HA-tagged SC expression on HEK293T was confirmed by flow cytometry (Fig. S7). Subsequent incubation of HEK293T-SC cells with StcE-ST resulted in successful and covalent surface conjugation, as verified by both western blotting and flow cytometry (Fig. 1*E*-*F*). Ligation was achieved with 0.1 μM StcE-ST, whereas higher concentrations (>2 μM) caused non-specific binding (Fig. 1*G*-*I*). These results validate the establishment of a controllable platform using engineered HEK293T-SC cells for the robust surface display of high-molecular-weight enzymes.

## Preparation and characterization of fusion cellular vesicles

Having established a platform for StcE display, we next evaluated the ability of the engineered HEK293T-StcE cells to remove mucins from tumor cell surfaces (Fig. 2*A*). Flow cytometry confirmed that HEK293T-StcE cells, effectively degraded MUC1 on HeLa cells (Fig. 2*B*). This system enabled controlled mucin degradation on HeLa cells through titration of StcE-ST concentrations (Fig. 2*C*).

Moreover, HEK293T-StcE cells also efficiently degraded mucins on the surface of both CT26 and 4T1 cells, indicating broad applicability (Fig. 2*D-G*). We then prepared nanovesicles (StcE-NVs) from these engineered cells via sonication and extrusion. The resulting StcE-NVs retained potent mucinase activity, successfully reducing MUC1 levels on HeLa cells, whereas control vesicles derived from StcE*-expressing cells (StcE*-NVs) showed no effect (Fig. S8). StcE-NVs maintained stable hydrolysis activity for at least one week when stored at 4°C (Fig. S9). However, StcE-NVs lacked tumor-targeting ability because they were derived from normal cells without inherent homing capacity, and StcE itself does not exhibit cell-type specificity.

To enhance the tumor targeting and therapeutic potential, StcE-NVs were fused with nCD47-NVs derived from 4T1/CT26-nCD47 cells to generate StcE-nCD47-FNVs, while StcE*-NVs were fused in parallel to obtain StcE*-nCD47-FNVs (Fig. 2*H*). StcE-nCD47-FNVs significantly depleted MUC1 from the surface of HeLa cells across adjustable fusion ratios (Fig. 2*I*). A 1:3 mass ratio (StcE-NVs to nCD47-NVs) was selected for subsequent studies, as it provided optimal mucinase activity and high nCD47 expression. Western blotting confirmed the presence of both nCD47 and StcE-ST in StcE-nCD47-FNVs, consistent with inheritance from the parental vesicles (Fig. 2*J*). Confocal microscopy further verified successful membrane fusion, showing co-localization of DiI-labeled nCD47-NVs (red) and DiO-labeled StcE-NVs (green) (Fig. 2*K*, S10*A*). Physical characterization revealed that StcE-nCD47-FNVs maintained a diameter of approximately 160 nm, a zeta potential of -25 mV, and a cup-shaped morphology, similar to the precursor vesicles (Fig. 2*L-M*, S10*B-D, S11*). Single-molecule localization microscopy further confirmed the co-display of nCD47 and StcE on individual vesicles, with cross-correlation analysis revealing significant nanoscale association within StcE-nCD47-FNVs (Fig. S12). Crucially, the enzymatic function was preserved post-fusion. Flow cytometry showed that the mucinase activity of StcE-nCD47-FNVs against 4T1 cell-surface mucins was comparable to that of StcE-NVs (Fig. 2*N*). This work developed mucin degradation StcE-NVs capable of fusing with other functional vesicles, such as nCD47-NVs, to create StcE-nCD47-FNVs with enhanced tumor-targeting capability and improved therapeutic payload delivery.

### StcE-nCD47-FNVs enhance tumor accumulation and improve systemic biocompatibility

High CD47 expression on tumor cells suppresses macrophage phagocytosis by engaging the SIRPα inhibitory receptor (31). StcE-nCD47-FNVs were designed to overcome this by simultaneously degrading the glycocalyx and blocking the CD47-SIRPα axis. First, we validated the binding specificity of the nCD47 component. CD47-knockdown (CD47KD) tumor cells were generated and characterized (Fig. 3*A-C*, S13). Immunofluorescence imaging showed that FITC-labeled nCD47-NVs bound efficiently to wild-type cells but minimally to CD47KD cells, confirming CD47-specific binding. StcE-nCD47-FNVs exhibited enhanced binding compared with nCD47-NVs, whereas StcE*-nCD47-FNVs were comparable to nCD47-NVs, indicating that the increased binding of StcE-nCD47-FNVs is primarily due to the enzymatic activity of StcE-mediated glycocalyx degradation (Fig. 3*D-E*, S14). We next examined whether enhanced binding translated into increased phagocytosis. Tumor cells pretreated with different NVs were co-incubated with M1 macrophages. StcE-nCD47-FNVs markedly increased phagocytosis index compared with nCD47-NVs, whereas StcE*-nCD47-FNVs failed to enhance phagocytosis and showed slightly lower activity (Fig. 3*F-G*). Consistently, treatment with the actin polymerization inhibitor Cytochalasin D markedly reduced macrophage-tumor cell fluorescence co-localization, whereas opsonization with an anti-EpCAM antibody enhanced macrophage engulfment. These findings confirmed that the observed co-localization represents phagocytic uptake of tumor cells (Fig. S15). Together, these results demonstrate that StcE-mediated glycocalyx degradation enhances CD47 targeting and promotes macrophage phagocytosis.

We next evaluated the biodistribution and biosafety of StcE-nCD47-FNVs *in vivo*. In CT26 tumor-bearing mice, Cy5.5-labeled nCD47-NVs and StcE-nCD47-FNVs exhibited sustained tumor accumulation, whereas free StcE was rapidly cleared from circulation. These results were further confirmed by *ex vivo* imaging of dissected tumor tissues (Fig. 3*H*). Fluorescence signals detected in major organs suggested that the vesicles were primarily cleared *via* hepatic clearance pathways (Fig. S16). Crucially, displaying StcE on StcE-nCD47-FNVs significantly mitigated its systemic toxicity. Briefly, mice treated with free StcE developed severe adverse effects, including hematological abnormalities (*e.g.*, decreased platelets), periocular inflammation, and hepatotoxicity, as indicated by elevated liver enzymes (ALT, AST, LDH) (Fig. 3*I-K*, S17, S18). In contrast, the StcE-nCD47-FNVs treatment group exhibited normal hematological and biochemical profiles, with no histopathological abnormalities observed in major organs. These *in vivo* safety findings were consistent with *in vitro* assays, in which FNVs possessed excellent hemocompatibility and minimal cytotoxicity, whereas free StcE induced erythrocyte hemolysis and reduced viability of bEnd.3 cells

(Fig. S19). Together, these findings indicate that StcE displayed on StcE-nCD47-FNVs enhances CD47 binding and promotes macrophage phagocytosis. The tumor-specific accumulation of StcE-nCD47-FNVs *in vivo* is critical for reducing StcE-associated toxicity.

### *In vivo* antitumor efficacy of StcE-nCD47-FNVs in a subcutaneous tumor model

Encouraged by *in vitro* findings, we next evaluated the therapeutic efficacy of StcE-nCD47-FNVs in CT26 tumor-bearing mice. On day 7 post-inoculation, mice were randomized into five treatment groups and dosed intravenously every other day: G1 (PBS), G2 (FNVs), G3 (StcE-FNVs, glycocalyx hydrolysis only), G4 (nCD47-FNVs, CD47 blockade only), and G5 (StcE-nCD47-FNVs, combination) (Fig. 4*A*). Mice in all groups were injected with 120 µL of vesicle suspension at 1 mg/mL, a dose selected based on preliminary optimization experiments evaluating both antitumor efficacy and systemic safety (Fig. S20). While control groups (G1, G2) exhibited rapid tumor growth, all treatment groups showed different level of inhibition. The single-modality treatments (G3 and G4) only moderately suppressed tumor progression. In contrast, the combination therapy in G5 produced a markedly potent anti-tumor effect, achieving a tumor inhibition rate of 95.83 ± 2.71%, (Fig. 4*B-C*, S21). This enhanced efficacy is attributed to a synergistic mechanism where initial nCD47 binding facilitates StcE-mediated hydrolysis of the glycocalyx, which in turn exposed new epitopes to improve overall vesicle binding. Importantly, this potent efficacy was achieved without inducing significant body weight loss, indicating a favorable safety profile for the treatment (Fig. 4*D*). Survival analysis further confirmed these results, as the G5 mice showed significantly prolonged survival compared to all other groups (Fig. 4*E*).

To elucidate the immunological mechanisms underlying the observed therapeutic efficacy, we performed a detailed analysis of the tumor microenvironment. Flow cytometry revealed a comprehensive remodeling of the immune landscape in G5 tumors. This included a polarization of macrophages toward a pro-inflammatory M1-like phenotype, an increased infiltration of cytotoxic $CD8^+$ T cells and NK cells, and a reduction in immunosuppressive regulatory T cells (Fig. 4*F-I*, S22-S26). Consistent with this pro-inflammatory shift, cytokine analysis showed an upregulation of IFN-γ and IL-6 alongside a downregulation of TGF-β and IL-10 (Fig. S27). Transcriptomic analysis provided deeper insight into these changes. Principal component analysis (PCA) showed a clear distinction between the G5 and control groups, with 852 differentially expressed genes identified

(Fig. S28*A*-*B*). Pathway analysis revealed that G5 treatment upregulated immune activation genes (Ifng, Ccl3) while downregulating genes associated with immunosuppression (Mmp23), proliferation (Egfr), and extracellular matrix (ECM) remodeling (Postn, Col6a3) (Fig. 4*J*). Furthermore, Gene Set enrichment analysis (GSEA) showed a negative enrichment negative enrichment for key oncogenic pathways, including PI3K-Akt, Wnt, and focal adhesion signaling (Fig. 4*K*-*L*, S28*C*-*E*). Collectively, these immune cellular and transcriptomic analyses confirm that StcE-nCD47-FNVs reverse immunosuppression and activate potent anti-tumor immune responses, highlighting the synergistic interplay between StcE, nCD47, and NVs.

To determine whether the catalytic activity of StcE and its co-display with nCD47 are required for the enhanced therapeutic efficacy, additional *in vivo* comparisons were performed in CT26 tumor-bearing mice (Fig. S30). StcE-nCD47-FNVs produced stronger tumor growth inhibition than nCD47-FNVs, whereas StcE*-nCD47-FNVs (lacking enzymatic activity) exhibited reduced therapeutic efficacy (Fig. S30*B*). Consistently, immunofluorescence staining and flow cytometry analysis revealed decreased mucin-associated signals on tumor cells in the StcE-nCD47-FNV-treated group (Fig. S29, S30*D, L*), confirming effective glycocalyx degradation *in vivo*. Moreover, the physical mixture of StcE-NVs and nCD47-NVs showed weaker tumor suppression than StcE-nCD47-FNVs, indicating that co-display of StcE and nCD47 on the same vesicle is required for optimal therapeutic efficacy. Together, these results demonstrate that the catalytic activity of StcE and its co-display with nCD47 on NVs are essential for the enhanced immunotherapeutic effect.

### ***In vivo* antitumor efficacy of StcE-nCD47-FNVs in a metastatic tumor model**

To evaluate the efficacy of StcE-nCD47-FNVs in a more stringent metastatic setting, we employed a 4T1 lung metastasis model. Mice were intravenously injected with luciferase-expressing 4T1 cells and subsequently randomized into five treatment groups: G1 (PBS), G2 (FNVs), G3 (StcE-FNVs), G4 (nCD47-FNVs), and G5 (StcE-nCD47-FNVs). Treatments were administered every two days, and tumor progression was monitored via *in vivo* bioluminescence imaging (Fig. 5*A*). After 21 days, both *in vivo* and *ex vivo* imaging revealed that the G5 (StcE-nCD47-FNVs) treatment exerted the most significant inhibitory effect on lung metastases (Fig. 5*B*). While the monotherapies (G3 and G4) provided a slight, limited therapeutic benefit, lungs from G5 group showed reduction in both the size and number of metastatic nodules, corresponding to a tumor inhibition rate of 92.90 ± 3.71%

(Fig. 5*C-E*, S31*A*). Histological analysis via H&E staining further confirmed these findings. Crucially, the survival rate for mice treated with StcE-nCD47-FNVs was 100% at day 35, underscoring the potent therapeutic efficacy of the combination therapy in a metastatic setting (Fig. 5*F*).

We next investigated whether the anti-metastatic efficacy of StcE-nCD47-FNVs was driven by a similar activation of the immune system. Immunofluorescence staining of lung tissue from the G5 treatment group confirmed a significant remodeling of the immune microenvironment. Macrophages repolarized toward a pro-inflammatory M1 phenotype, evidenced by an increase in $CD86^+$ cells and a decrease in $CD206^+$ M2 cells (Fig. 5*G*). Furthermore, treatment with StcE-nCD47-FNVs significantly enhanced the infiltration of $CD8^+$ T cells into the lung tissue (Fig. S31*B*). This cellular reprogramming was accompanied by a robust change in the cytokine profile. The lungs of treated mice showed a significant upregulation of pro-inflammatory cytokines, including IFN-γ, TNF-α, and IL-1β, and a concurrent downregulation of the immunosuppressive cytokine IL-10 (Fig. 5*H-K*). Collectively, these results demonstrate that StcE-nCD47-FNVs effectively reverses the immunosuppressive microenvironment in lung metastases. This potent immune activation, characterized by M1 macrophage polarization and cytotoxic T cell infiltration, underlies the therapy’s ability to eliminate metastatic tumors and prolong survival.

## Discussion

In this study, we developed a multifunctional fused cell-derived vesicle platform, StcE-nCD47-FNVs, that synergistically overcame tumor immune evasion by combining glycocalyx degradation with CD47 checkpoint blockade. StcE-NVs were first generated using the SpyTag–SpyCatcher system to efficiently hydrolyze mucins, and subsequently fused with nCD47-NVs, derived from engineered tumor cells, to form StcE-nCD47-FNVs with well-defined physicochemical properties while retaining mucin hydrolysis activity. By degrading the mucin barrier, StcE-nCD47-FNVs enhanced the binding of nCD47 to tumor-cell CD47, which blocked the CD47-SIRPα axis and significantly promoted macrophage phagocytosis. Furthermore, StcE-nCD47-FNVs possessed superior tumor accumulation and safety compared to free StcE *in vivo*. In two murine tumor models, StcE-nCD47-FNVs markedly inhibited primary tumor growth and metastasis, prolonged survival, and remodeled the tumor microenvironment by promoting M1 macrophage polarization and cytotoxic $CD8^+$ T cell infiltration.

The tumor glycocalyx has recently emerged as a critical regulator of immune evasion (32), and

StcE has been proposed as a potential tool to enhance cancer immunotherapy (14). However, its bacterial origin and lack of intrinsic targeting raise potential safety concerns. Previous studies explored different engineering strategies: Bertozzi et al. designed a HER2-targeted StcE variant to selectively remove mucins on HER2-positive tumor cells while reducing catalytic activity (13), whereas Paszek et al. retained full enzymatic activity to maximize O-glycan cleavage, with potential risk of nonspecific degradation (33). In the present work, we combined these insights to balance activity and specificity, retaining StcE's catalytic function while removing the C-terminal X409 lectin domain responsible for nonspecific binding. This design preserved mucin-hydrolyzing activity while reducing unintended interactions, providing a practical strategy for *in vivo* application.

The NVs derived from natural membranes through differential centrifugation, sonication, and extrusion offer a versatile platform for *in vivo* application due to their low immunogenicity and relatively long circulation (34). The surface of NVs is readily modifiable, and in this work, SpyTag/SpyCatcher-mediated conjugation enabled site-specific covalent display of StcE while maintaining enzymatic activity. Moreover, NVs can present multiple functional proteins on a single carrier via fusion-based assembly, simplifying the construction of multifunctional therapeutics and lowering technical barriers. The favorable tumor accumulation of StcE-nCD47-FNVs likely reflects both nCD47-mediated targeting and the homologous properties of vesicles derived from parental cells (18, 24). This modular strategy could be extended to other nanoplatforms to enable rapid functionalization with diverse proteins, including high-molecular-weight or potentially off-target toxic therapeutics (35).

Combining glycocalyx hydrolysis with checkpoint blockade produces measurable antitumor effects in both tumor models. Analysis of tumor samples confirmed that StcE-nCD47-FNVs effectively synergized the functions of StcE and nCD47, as evidenced by increased infiltration of $CD86^+$ macrophages and elevated levels of inflammatory cytokines, which correlated with tumor suppression. Additionally, infiltration of cytotoxic lymphocytes and NK cells was also elevated, suggesting that glycocalyx hydrolysis may expose additional tumor antigens and potentially facilitate broader immune recognition. Transcriptomic analysis further supported this interpretation, showing downregulation of pathways such as PI3K-Akt and Wnt, consistent with comprehensive remodeling of the tumor microenvironment. Taken together, these findings highlight StcE-nCD47-FNVs as a modular and generalizable platform for integrating glycocalyx degradation with other therapeutic modalities. Future studies may focus on customizing NVs for personalized glycocalyx removal, which could be applicable not only to cancer but also to other diseases characterized by aberrant glycocalyx expression. The modular platform could also be explored for the co-display of additional functional proteins. Further experiments in preclinical models will be necessary to assess whether NVs have the potential to join other nanomedicines, such as clinically approved liposomes, as frontline therapeutics.

## Materials and Methods

### Generation of stable cell lines

The SpyCatcher or nCD47 construct was inserted into a linearized pLenti-EGFP-CMV lentiviral expression vector. Replication-deficient lentivirus was produced by transfecting HEK293T cells at 90% confluency in 6-well plates with a plasmid mixture containing 0.75 µg of psPAX2, 0.25 µg of pMD2.G, and 1 µg of the plasmid encoding the gene of interest. The viral supernatant was collected 48 h post-transfection and filtered through a 0.45 µm membrane. For infection, the filtrate was combined with an equal volume of fresh medium containing 10 µg/mL polybrene and used to infect the target cells. HEK293T cells were used to generate a SpyCatcher stable cell line, whereas 4T1 and CT26 cells were used to establish nCD47-expressing stable cell lines. At 48 h post-infection, cells were harvested, and the GFP-positive population was isolated by fluorescence-activated cell sorting (FACS) using a CytoFLEX SRT instrument (Beckman Coulter).

### Conjugation of SpyCatcher with SpyTag

For *in vitro* conjugation, recombinant SpyCatcher (SC) and SpyTag (ST)-labeled StcE variants were incubated in PBS (pH 7.4) containing 1% (w/v) BSA on ice for 25 min. Reactions were quenched by adding 5× SDS-PAGE loading buffer and heating at 95 °C for 5 min. Conjugation efficiency was assessed by 8% SDS-PAGE analysis. For cell-surface conjugation, HEK293T-SC cells were detached using 0.25% trypsin and incubated with ST-labeled StcE variants in PBS containing 1% BSA for 25 min on ice with periodic mixing. Cells were washed twice with PBS to remove unbound protein. Conjugation efficiency was quantified by staining with an APC–anti-His-tag antibody followed by flow cytometry analysis (FlowJo software).

### Flow cytometry analysis of demucinated tumor cells

Tumor cells were treated with either purified StcE variants or with HEK293T-SC cells/vesicles that had been pre-conjugated with ST-labeled proteins. For the assay, one million tumor cells were incubated in 1 mL of complete medium or PBS with varying purified protein and CVs at 37 °C for 1 h. HEK293T cells expressing StcE were added at a 2:1 ratio relative to tumor cells at 37 °C and 20 rpm for 1 h. After treatment, cells were washed with ice-cold FACS buffer and stained with fluorophore-conjugated antibodies for 30 min at 4 °C. For co-culture conditions involving HEK293T-StcE cells, the EGFP-negative population was gated to quantify mucin levels on tumor cell surfaces. Data were acquired on a flow cytometer and analyzed using FlowJo software.

### Western blot analysis of bio-conjugation on the surface of cells and NVs

To analyze surface conjugation, cells and cellular nanovesicles (NVs) were lysed in RIPA buffer. Total protein concentration was quantified using a bicinchoninic acid (BCA) assay kit (Thermo Fisher). Equal amounts of denatured protein lysate were separated on a 10% SDS-polyacrylamide gel and subsequently transferred to a nitrocellulose membrane using an eBlot™ L1 system (Genscript). The membrane was blocked with 5% (w/v) non-fat dry milk in TBST for 1 h at room temperature. Membranes were then incubated with primary antibodies overnight at 4 °C, followed by incubation with an HRP-conjugated secondary antibody for 1 h at room temperature. Blots were visualized using an Azure Imager C600.

### Preparation and characterization of nanovesicles

Cell membrane nanovesicles (NVs) were prepared from HEK293T-SC, HEK293T-StcE, 4T1, 4T1-nCD47, CT26, and CT26-nCD47 cells. Cells were harvested and subjected to three rapid freeze–thaw cycles using liquid nitrogen for freezing and a room-temperature water bath for thawing to disrupt cellular structures. The resulting lysate was clarified by centrifugation at 4,000 × g for 45 min at 4 °C to remove intact cells and large debris. The supernatant was subsequently ultracentrifuged at 100,000 × g for 1 h at 4 °C to pellet crude membrane vesicles. The pellet was resuspended in PBS and briefly sonicated on ice (50 W, 2 s on, 4 s off pulse cycle for 5 min) to disperse membrane fragments. The suspension was then sequentially extruded (10 passes each) through 200 nm and 100 nm polycarbonate membranes using a mini-extruder to generate vesicles with a relatively uniform size distribution. Single-source vesicles were designated as NVs (HEK293T, 4T1, CT26), StcE-NVs (HEK293T-StcE), and nCD47-NVs (4T1/CT26-nCD47). Fused nanovesicles (FNVs) were generated by mixing NVs at defined mass ratios (Supplementary *Table 2*), followed by sonication and extrusion. The resulting formulations included FNVs, StcE-FNVs, nCD47-FNVs, and StcE-nCD47-FNVs. Protein concentration was determined using a BCA assay (Thermo Fisher). For membrane fusion analysis, StcE-NVs and nCD47-NVs were separately labeled with lipophilic dyes and then mixed at defined ratios. The mixture was incubated at 37 °C, followed by observation using confocal laser scanning microscopy (36). For TEM analysis, vesicles were stained with 2% phosphotungstic acid. Hydrodynamic size and zeta potential were measured by dynamic light scattering (DLS) using a Malvern Zetasizer.

### Cell binding assay

CD47-knockdown (CD47 KD) cells were generated using a lentiviral shRNA system targeting CD47, and knockdown efficiency was validated by flow cytometry and qPCR. CT26, CT26 CD47KD, 4T1, and 4T1 CD47KD cells were seeded into 8-well confocal dishes at a density of $5 \times 10^4$ cells/well. After 12 h, each well was treated with 120 μg of the corresponding vesicle formulation (NVs, nCD47-NVs, StcE*-nCD47-FNVs and StcE-nCD47-FNVs) in 300 μL of medium for 1 h. Following treatment, the cells were washed twice with PBS and fixed with 4% paraformaldehyde for 15 min. The cell membranes were then stained with WGA-Alexa Fluor 647 (WGA-AF647) for 15 min at room temperature. After washing, cells were blocked with 5% BSA in PBS for 1 h at room temperature and then incubated with an anti-HA primary antibody overnight at 4°C. The next day, cells were washed twice with PBS and incubated with a FITC-conjugated secondary antibody for 1 h at room temperature. Finally, nuclei were counterstained with DAPI for 15 min. After a final wash, serum-free medium was added to each well, and images were acquired using a Zeiss LSM 980 confocal microscope equipped with a 40x objective.

### Phagocytosis assay

RAW264.7 macrophages were stimulated with lipopolysaccharide (LPS, 200 ng/mL) for 24 h, labeled with CFSE (eBioscience™), and seeded into 4-chamber confocal dishes. In parallel, 4T1 or CT26 cancer cells were harvested, stained with eFluor™ 670 proliferation dye, and treated with the indicated nanovesicle formulations for 3 h at 37°C. These vesicle-treated cancer cells were then washed and co-cultured with the prepared RAW264.7 macrophages for 6 h. After co-incubation, the cells were washed with PBS, fixed with 4% paraformaldehyde, and imaged on a Zeiss LSM980 confocal microscope equipped with a 63x objective. Images were subsequently processed and analyzed using Fiji software. For antibody-dependent cell-mediated phagocytosis (ADCP) assay, NVs pretreated 4T1 cells were opsonized in serum-free medium for 30 min on ice with 10 μg/ml anti-EpCAM (Thermal Fisher), or with mouse IgG2a isotype control antibody (Thermal Fisher). Then washed and co-cultured with the prepared RAW264.7 macrophages for 6 h.

### Animal model for *in vivo* experiments

Female BALB/c mice (6-8 weeks) were purchased from GemPharmatech Co., Ltd. and housed in a specific pathogen-free (SPF) facility. All animal procedures were conducted in accordance with guidelines approved by the Regional Ethics Committee for Animal Experiments at Shenzhen Bay Laboratory (Permit No. AERL202401). For the subcutaneous tumor model, mice were injected in the right flank with $5 \times 10^5$ CT26 cells. *In vivo* biodistribution studies were performed 10 days post-inoculation. Therapeutic efficacy studies were initiated 7 days post-inoculation. For the lung metastasis model, mice were injected via the tail vein with $2 \times 10^5$ 4T1-luciferase expressing (4T1-luc) cells. Metastatic progression was monitored by measuring bioluminescence signals from the thoracic region on days 0, 9, 15, and 21 using an *in vivo* imaging system (Xenogen Corp).

### *In vivo* biodistribution and biocompatibility of StcE-nCD47-FNVs

For fluorescent labeling, StcE protein was conjugated with NHS-Cy5.5 at a protein-to-dye molar ratio of 1:10 by incubation at 37 °C for 2 h. Unconjugated dye was removed using a desalting column, and the labeled protein was concentrated to 1 mg/mL using a 10 kDa molecular weight cutoff ultrafiltration device. Nanovesicle formulations (StcE-NVs, CT26-nCD47-NVs, and CT26-StcE-nCD47-FNVs) were labeled by incubating 1 mg vesicles with 100 μg DSPE-PEG-Cy5.5 in 1 mL PBS at 37 °C for 20 min with continuous shaking, followed by 10 min bath sonication to facilitate membrane insertion (24). Biodistribution studies were conducted in CT26 tumor-bearing BALB/c mice 10 days after tumor cell inoculation. Mice were randomly assigned to four groups (*n* = 3 per group) and intravenously injected with Cy5.5-labeled StcE, StcE-NVs, CT26-nCD47-NVs, or

CT26-StcE-nCD47-FNVs. Whole-body fluorescence images were acquired at 0.5, 1, 2, 4, 6, 12, 24, 36, and 48 h post-injection using an *in vivo* imaging system. At 48 h, mice were euthanized, and tumors and major organs were harvested for *ex vivo* fluorescence quantification. To evaluate potential systemic toxicity, CT26 tumor-bearing mice received intravenous injections of StcE or CT26-StcE-nCD47-FNVs. At the study endpoint, blood samples were collected for complete blood count and serum biochemical analysis (*n* = 3 per group). Major organs, including the heart, liver, spleen, lungs, and kidneys, were harvested, fixed in 4% paraformaldehyde, and subjected to hematoxylin and eosin staining for histopathological analysis.

### *In vivo* therapeutic efficacy

Seven days after tumor inoculation, CT26 tumor-bearing mice were randomized into five treatment groups to receive intravenous injections of: PBS (vehicle control, n = 13), CT26-FNVs (n = 10), CT26-StcE-FNVs (n = 10), CT26-nCD47-NVs (n = 10), or CT26-StcE-nCD47-FNVs (n = 13). Each dose consisted of a 120 µL injection volume containing 120 µg of the respective agent. Treatments were administered every other day for a total of six doses. Body weight and tumor volume were monitored every other day starting on day 5. Mice were euthanized when tumor volume exceeded 1500 mm$^3$, which was defined as the endpoint for survival analysis. A subset of mice from each group was monitored for a long-term survival study. Separate groups of mice were used for different analyses, including 4 mice per group for flow cytometry and ELISA, and 6 mice per group for tumor growth monitoring and survival analysis. In addition, 3 mice from the PBS and CT26-StcE-nCD47-FNVs groups were used for RNA sequencing.

For the lung metastasis model, 4T1 tumor-bearing mice were similarly assigned to five groups (*n* = 10 per group) and treated with the indicated formulations following the same dosing regimen. Tumor progression was monitored by bioluminescence imaging after intraperitoneal injection of 150 µL D-luciferin at 20 mg/mL (Beyotime, ST196) on days 0, 9, 15, and 21, using an *in vivo* imaging system (Xenogen Corp). Separate groups of mice were used for different analyses, including 5 mice per group for immunofluorescence and RT-qPCR, and 5 mice per group for survival monitoring.

### Flow cytometry analysis of intratumoral immune cells

On day 19 post-inoculation, CT26 tumors were excised and dissociated into single-cell suspensions for immune profiling. Tissues were mechanically minced and then enzymatically digested for 40 min in a buffer containing DNase I (25 U/mL), Collagenase (0.2 mg/mL), and Hyaluronidase (0.1 mg/mL). The digest was further processed using a gentleMACS Dissociator. The resulting cell suspension was filtered through a 70 μm cell strainer, and contaminating red blood cells were removed by incubation with RBC Lysis Buffer (Solarbio). After quantification, $2 \times 10^6$ cells per sample were stained with antibody panels to identify T cell, macrophage, and NK cell populations, as detailed in the Table S1 and Fig. S22-S26.

### RNA sequencing

On day 12, tumor tissues were harvested from three randomly selected mice from the control and CT26-StcE-nCD47-FNVs treatment groups. The tissues were immediately snap-frozen and stored at -80°C. Total RNA extraction, library preparation, sequencing, and bioinformatics analysis were performed by Novogene Co., Ltd. (Beijing, China).

### Reverse-transcription quantitative polymerase chain reaction (RT-qPCR) assay

For )reverse-transcription quantitative polymerase chain reaction (RT-qPCR) assay, mRNA levels of inflammatory cytokines in 4T1 lung tissues were measured. Total RNA was extracted from cryopreserved tissues using a commercial RNA extraction kit, and cDNA was subsequently synthesized using the iScript™ cDNA Synthesis Kit (Bio-Rad). qRT-PCR was performed using SYBR Green SuperPremix on a CFX96 Real-Time System (Bio-Rad). Gene expression was normalized to the housekeeping gene GAPDH, and relative expression levels were calculated using the $2^{-\Delta\Delta CT}$ method. All primers (Table S2) were synthesized by BGI Co., Ltd.

### Immunofluorescence for 4T1 lung metastasis mouse model

Lung tissues were collected from the 4T1 lung metastasis mouse model, fixed overnight in 4% paraformaldehyde at 4°C, and embedded in paraffin. Paraffin-embedded sections were deparaffinized, rehydrated, and subjected to antigen retrieval. Sections were then blocked with serum for 1 h at room temperature and incubated overnight at 4°C with primary antibodies against CD4, CD8, CD206, or CD86. After washing, sections were incubated with corresponding fluorophore-conjugated secondary antibodies for 1 h. Nuclei were counterstained with DAPI, and images were acquired on an Olympus VS200 fluorescence microscope.

### Statistical analyses

Data are presented as mean ± standard deviation (SD) unless otherwise specified. Statistical analyses were performed using GraphPad Prism (v. 10.1.2). Comparisons between multiple groups were conducted using a one-way analysis of variance (ANOVA) followed by Tukey's post hoc test. For experiments with two independent variables, a two-way ANOVA with Tukey's post hoc test was used. Survival curves were generated using the Kaplan-Meier method and compared using the log-rank (Mantel-Cox) test. A *P-value* $< 0.05$ was considered statistically significant. Significance levels are denoted as follows: *$P < 0.05$, **$P < 0.01$, and ***$P < 0.001$.

**Data, materials, and software availability.** All study data are included in the article and/or *SI Appendix*.

## Acknowledgements

We would like to thank Prof. Yandong Yin and Yue Xin from Shenzhen Bay Laboratory for technical support on single-molecule imaging experiments. This work was supported by the Shenzhen Medical Research Fund (No. B2502017 to L.R.), National Key R&D Program of China (Nos. 2024YFC3407200 to Y.G., and 2025YFA0923000 to L.R.), the National Natural Science Foundation of China (Nos. 82222035, 82372106 to L.R., 22277080, 92478103 to Y.G., and 82502547 to Y.P.), the and the Major Program of Shenzhen Bay Laboratory (No. S241101001 to Y.G.).

## Author Contributions

L.R. and Y.G. conceived the study. X.G. and S.L. designed the experiments. X.G. and S.L. performed the experiments. X.G. and S.L. analyzed the data. X.G., S.L., and Y.W. wrote the manuscript. All authors have given approval to the final version of the manuscript.

## Competing Interests

The authors have filed a patent on this work and declare no other conflict of interest in this work.

## References

1. K. Aliazis *et al.*, The tumor microenvironment's role in the response to immune checkpoint blockade. *Nat. Cancer* **6**, 924–937 (2025).
2. M. Y. Feng *et al.*, Phagocytosis checkpoints as new targets for cancer immunotherapy. *Nat. Rev. Cancer* **19**, 568–586 (2019).
3. M. E. W. Logtenberg, F. A. Scheeren, T. N. Schumacher, The CD47-SIRPα immune checkpoint. *Immunity* **52**, 742–752 (2020).
4. R. Upton *et al.*, Combining CD47 blockade with trastuzumab eliminates HER2-positive breast cancer cells and overcomes trastuzumab tolerance. *Proc. Natl. Acad. Sci.* **118**, e2026849118 (2021).
5. R. Advani *et al.*, CD47 blockade by Hu5F9-G4 and rituximab in non-Hodgkin's lymphoma. *N. Engl. J. Med.* **379**, 1711–1721 (2018).
6. C. R. Shurer *et al.*, Physical principles of membrane shape regulation by the glycocalyx. *Cell* **177**, 1757–1770 (2019).
7. J. C. H. Kuo, J. G. Gandhi, R. N. Zia, M. J. Paszek, Physical biology of the cancer cell glycocalyx. *Nat. Phys.* **14**, 658–669 (2018).
8. A. P. Corfield, Mucins: a biologically relevant glycan barrier in mucosal protection. *Biochim. Biophys. Acta, Gen. Subj.* **1850**, 236–252 (2015).
9. L. Z. Mi *et al.*, Simultaneous visualization of the extracellular and cytoplasmic domains of the epidermal growth factor receptor. *Nat. Struct. Mol. Biol.* **18**, 984–989 (2011).
10. D. Y. W. Lin *et al.*, The PD-1/PD-L1 complex resembles the antigen-binding Fv domains of antibodies and T cell receptors. *Proc. Natl. Acad. Sci.* **105**, 3011–3016 (2008).
11. G. Fenalti *et al.*, Structure of the human marker of self 5-transmembrane receptor CD47. *Nat. Commun.* **12**, 5218 (2021).
12. C. V. Rao *et al.*, Small-molecule inhibition of GCNT3 disrupts mucin biosynthesis and malignant cellular behaviors in pancreatic cancer. *Cancer Res.* **76**, 1965–1974 (2016).
13. K. Pedram *et al.*, Design of a mucin-selective protease for targeted degradation of cancer-associated mucins. *Nat. Biotechnol.* **42**, 597–607 (2024).
14. S. A. Malaker *et al.*, The mucin-selective protease StcE enables molecular and functional analysis of human cancer-associated mucins. *Proc. Natl. Acad. Sci.* **116**, 7278–7287 (2019).
15. N. Villalba, S. Baby, S. Y. Yuan, The endothelial glycocalyx as a double-edged sword in microvascular homeostasis and pathogenesis. *Frontiers in Cell and Developmental Biology* **9**, 711003 (2021).
16. R. L. Szabady, M. A. Lokuta, K. B. Walters, A. Huttenlocher, R. A. Welch, Modulation of neutrophil function by a secreted mucinase of escherichia coli O157:H7. *PLoS Pathog.* **5**, e1000320 (2009).
17. G. van Niel, G. D'Angelo, G. Raposo, Shedding light on the cell biology of extracellular vesicles. *Nat. Rev. Mol. Cell Biol.* **19**, 213–228 (2018).
18. D. W. Greening *et al.*, Clinical relevance of extracellular vesicles in cancer — therapeutic and diagnostic potential. *Nat. Rev. Clin. Oncol.* **22**, 924–952 (2025).
19. X. Y. Lin, L. D. Yue, K. Cheng, L. Rao, Engineering cellular vesicles for immunotherapy. *Acc. Mater. Res.* **6**, 327–339 (2025).
20. C. C. Zhao *et al.*, Vesicular antibodies: shedding light on antibody therapeutics with cell

membrane nanotechnology. *Adv. Mater.* **35**, e2207875 (2023).

21. Y. Wen *et al.*, Cell-derived nanovesicles prepared by membrane extrusion are good substitutes for natural extracellular vesicles. *Extracell Vesicle* **1**, 100004 (2022).
22. G. Walsh, Biopharmaceutical benchmarks 2018. *Nat. Biotechnol.* **36**, 1136–1145 (2018).
23. K. Lang, J. W. Chin, Cellular incorporation of unnatural amino acids and bioorthogonal labeling of proteins. *Chem. Rev.* **114**, 4764–4806 (2014).
24. J. C. Wu, H. L. Lu, X. M. Xu, L. Rao, Y. Ge, Engineered cellular vesicles displaying glycosylated nanobodies for cancer immunotherapy. *Angew. Chem. Int. Ed.* **63**, e202404889 (2024).
25. B. Zakeri *et al.*, Peptide tag forming a rapid covalent bond to a protein, through engineering a bacterial adhesin. *Proc. Natl. Acad. Sci.* **109**, 690–697 (2012).
26. G. Kim *et al.*, Engineering modular enzyme assembly: synthetic interface strategies for natural products biosynthesis applications. *Nat. Prod. Rep.* **42**, 1489–1506 (2025).
27. D. P. Arnold, Y. X. Xu, S. C. Takatori, Antibody binding reports spatial heterogeneities in cell membrane organization. *Nat. Commun.* **14**, 2884 (2023).
28. M. A. Goyette *et al.*, Cancer-stromal cell interactions in breast cancer brain metastases induce glycocalyx- mediated resistance to HER2targeting therapies. *Proc. Natl. Acad. Sci.* **121**, e2322688121 (2024).
29. Y. Zhou *et al.*, T Cell-derived apoptotic extracellular vesicles hydrolyze cGAMP to alleviate radiation enteritis via surface enzyme ENPP1. *Adv. Sci.* **11**, e2401634 (2024).
30. C. Kofoed *et al.*, Programmable protein ligation on cell surfaces. *Nature* **645**, 793–800 (2025).
31. S. B. Willingham *et al.*, The CD47-signal regulatory protein alpha (SIRPa) interaction is a therapeutic target for human solid tumors. *Proc. Natl. Acad. Sci.* **109**, 6662–6667 (2012).
32. E. Rodríguez, S. T. T. Schetters, Y. van Kooyk, The tumour glyco-code as a novel immune checkpoint for immunotherapy. *Nat. Rev. Immunol.* **18**, 204–211 (2018).
33. S. Park *et al.*, Immunoengineering can overcome the glycocalyx armour of cancer cells. *Nat. Mater.* **23**, 429–438 (2024).
34. J. Lai *et al.*, Triple Hybrid Cellular Nanovesicles Promote Cardiac Repair after Ischemic Reperfusion. *ACS Nano* **18**, 4443–4455 (2024).
35. X. Xiong *et al.*, Neoantigen-based cancer vaccination using chimeric RNA-loaded dendritic cell-derived extracellular vesicles. *J. Extracell. Vesicles* **11**, e12243 (2022).
36. L. Rao *et al.*, Hybrid cellular membrane nanovesicles amplify macrophage immune responses against cancer recurrence and metastasis. *Nat. Commun.* **11**, 4909 (2020).

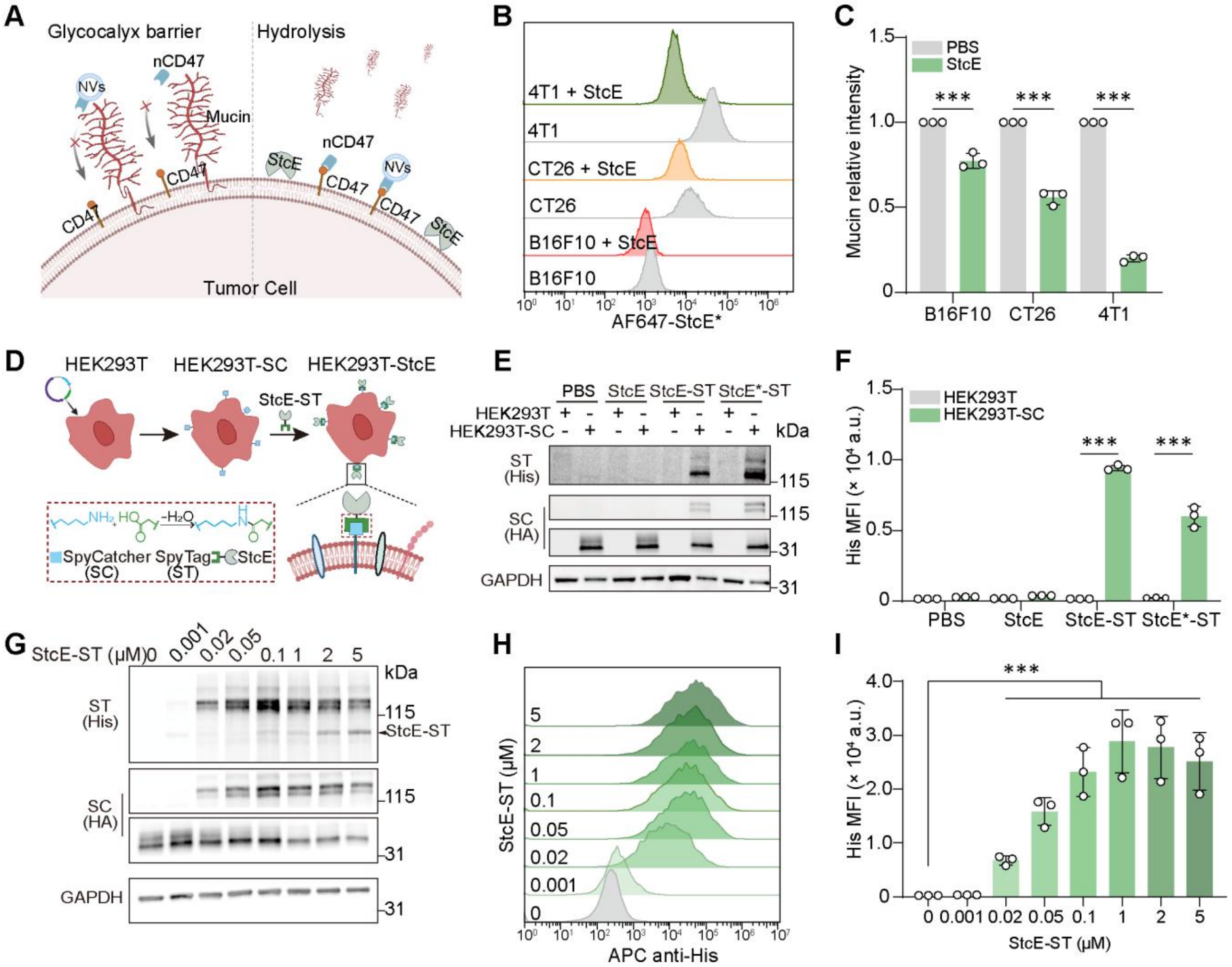

**Fig. 1. Bioconjugation display of mucinase StcE on HEK293T cell surfaces.** (*A*) Schematic illustration of mucinase-mediated degradation of the glycocalyx barrier, exposing the CD47 immune checkpoint to enhance binding of anti-CD47 nanobody (nCD47) or nCD47-conjugated NVs. (*B*) Flow cytometry analysis and (*C*) mean fluorescence intensity (MFI) quantification of mucin residues in the indicated cells treated with StcE, detected by Alexa Fluor 647 (AF647)-StcE* staining. (*D*) Schematic illustration of the bioconjugation reaction via SpyTag (ST)-SpyCatcher (SC) on SC-expressing HEK293T cells. (*E*) Western blot analysis of His- and HA-tagged proteins after incubation of StcE, StcE-ST, or StcE*-ST with HEK293T or HEK293T-SC cells. (*F*) MFI quantification of His-tagged proteins on cell surfaces after incubation with StcE, StcE-ST, or StcE*-ST, analyzed by live-cell flow cytometry using APC anti-His staining. Representative flow cytometry plots are shown in Fig. S36*A*. (*G*) Western blot analysis of His-tagged StcE-ST on HEK293T-SC cells after incubation with increasing concentrations of StcE-ST (0-5 μM). (*H*) Flow cytometry analysis and (*I*) MFI quantification of His-tagged StcE-ST on SC-expressing cells after incubation with increasing concentrations of StcE-ST

(0-5 μM). StcE*: inactive point mutant. Data are presented as mean ± S.D. (*n* = 3).

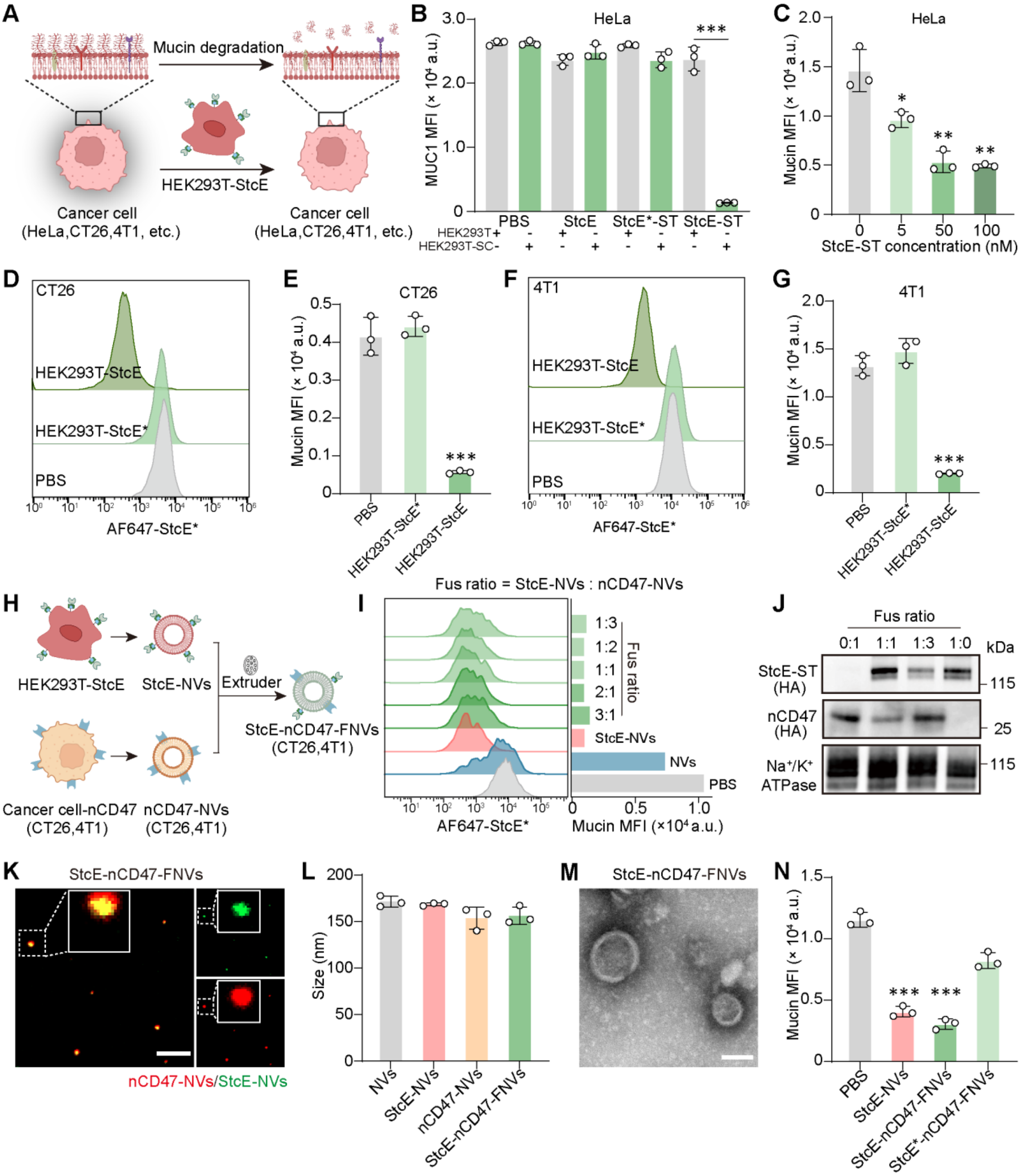

**Fig. 2. Preparation and characterization of multifunctional NVs.** (*A*) Schematic illustration of mucin degradation on cancer cell surfaces by HEK293T-StcE cells. (*B*) Mean fluorescence intensity (MFI) quantification of MUC1 on HeLa cells after incubation with HEK293T-StcE cells for 1 h, analyzed by live-cell flow cytometry using PE anti-MUC1 staining. (*C*) MFI quantification of mucin on HeLa cells after incubation with HEK293T-SpyCatcher (SC) cells conjugated with StcE-SpyTag (ST) at the indicated concentrations (5-100 nM) for 1 h, analyzed by live-cell flow cytometry with Alexa Fluor

647 (AF647)-StcE* staining. (*D*) Flow cytometry analysis and (*E*) MFI quantification of mucin on CT26 cells after incubation with HEK293T-StcE cells, detected by AF647-StcE* staining. (*F*) Flow cytometry analysis and (*G*) MFI quantification of mucin on 4T1 cells after incubation with HEK293T-StcE cells, detected by AF647-StcE* staining. (*H*) Schematic illustration of the preparation of genetically programmable StcE-nCD47-FNVs. (*I*) MFI quantification of MUC1 on HeLa cells after incubation with StcE-nCD47-FNVs at different fusion ratios, analyzed by live-cell flow cytometry with PE anti-MUC1 staining. NVs are derived from HEK293T cells. (*J*) Western blot analysis of nCD47 and StcE-ST in nCD47-NVs, StcE-nCD47-FNVs (fusion ratio = StcE-NVs: nCD47-NVs), and StcE-NVs. (*K*) Confocal laser scanning microscopy (CLSM) images showing fusion of DiI-labeled nCD47-NVs (red) with DiO-labeled StcE-NVs (green). The appearance of a yellow signal indicates co-localization and successful fusion to form StcE-nCD47-FNVs. Scale bar, 5 µm. (*L*) Size distribution of NVs (derived from CT26 cells), StcE-NVs, nCD47-NVs, and StcE-nCD47-FNVs. (*M*) Transmission electron microscopy (TEM) image of StcE-nCD47-FNVs. Scale bar, 50 nm. (*N*) MFI quantification of mucin on CT26 cells after incubation with StcE-nCD47-FNVs at a 1:3 fusion ratio, analyzed by live-cell flow cytometry with AF647-StcE* staining. StcE*: inactive point mutant. Data are presented as mean ± S.D. (*n* = 3). All nCD47-NVs are from CT26-nCD47 cells. Representative flow cytometry plots in *B, C, N* are shown in Fig. S36*B-D.*

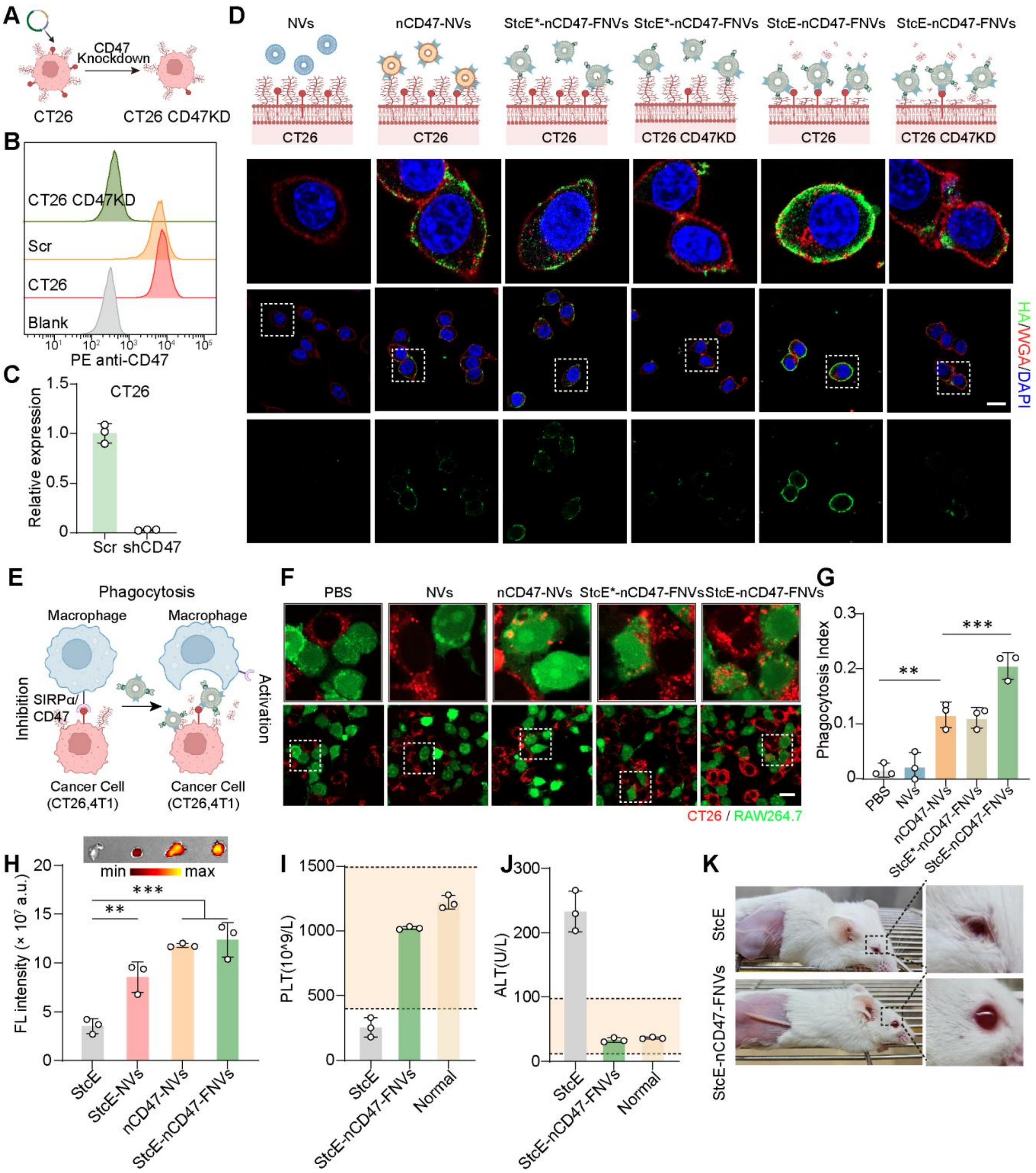

**Fig. 3. StcE-nCD47-FNVs for targeted CD47 checkpoint blockade and biocompatibility assessment.** (*A*) Schematic illustration of shRNA-mediated knockdown of CD47 expression in CT26 cells. (*B*) Flow cytometry analysis of CD47 protein levels in CT26 cells stably transfected with shScramble (shScr) or shCD47 RNA. (*C*) qPCR quantification of CD47 mRNA levels in CT26 cells stably transfected with shScr or shCD47 RNA. (*D*) Confocal imaging of nCD47-NVs or StcE-nCD47-FNVs binding to CD47 on CT26 cell surfaces. Scale bar, 20 μm. Representative images are derived from Supplementary Fig.

S14. (*E*) Schematic illustration showing how StcE-nCD47-FNVs overcome the CD47-SIRPα immune checkpoint to promote phagocytosis. StcE-nCD47-FNVs first degrade the tumor glycocalyx, enabling access to and blockade of the CD47, thereby triggering macrophage-mediated phagocytosis of cancer cells. (*F*) Fluorescence images of phagocytosis assays induced by the indicated NVs. RAW264.7 macrophages were stained with CFSE (green), and CT26 cells with eFluor670 (red). Scale bar, 20 μm. (*G*) Quantification of the phagocytosis index of CT26 cells by RAW264.7 macrophages. The phagocytosis index was calculated as the number of CFSE$^+$ tumor cells engulfed per 50 macrophages. (*H*) *In vivo* imaging and quantification of CT26 tumors from subcutaneous xenografts 48 h after intravenous injection of Cy5.5-labeled StcE, StcE-NVs, nCD47-NVs, or StcE-nCD47-FNVs at equivalent protein concentrations. (*I-J*) Hematological and serum biochemical analyses of treated mice. Shown are platelet (PLT) counts and alanine aminotransferase (ALT) levels, with normal ranges indicated by orange shading. (*K*) Representative photographs of ocular inflammation in mice following the different treatments. Data are presented as mean ± S.D. ($n = 3$) $*P < 0.05$, $**P < 0.01$, $***P < 0.001$. NVs and nCD47-NVs are from CT26 and CT26-nCD47 cells.

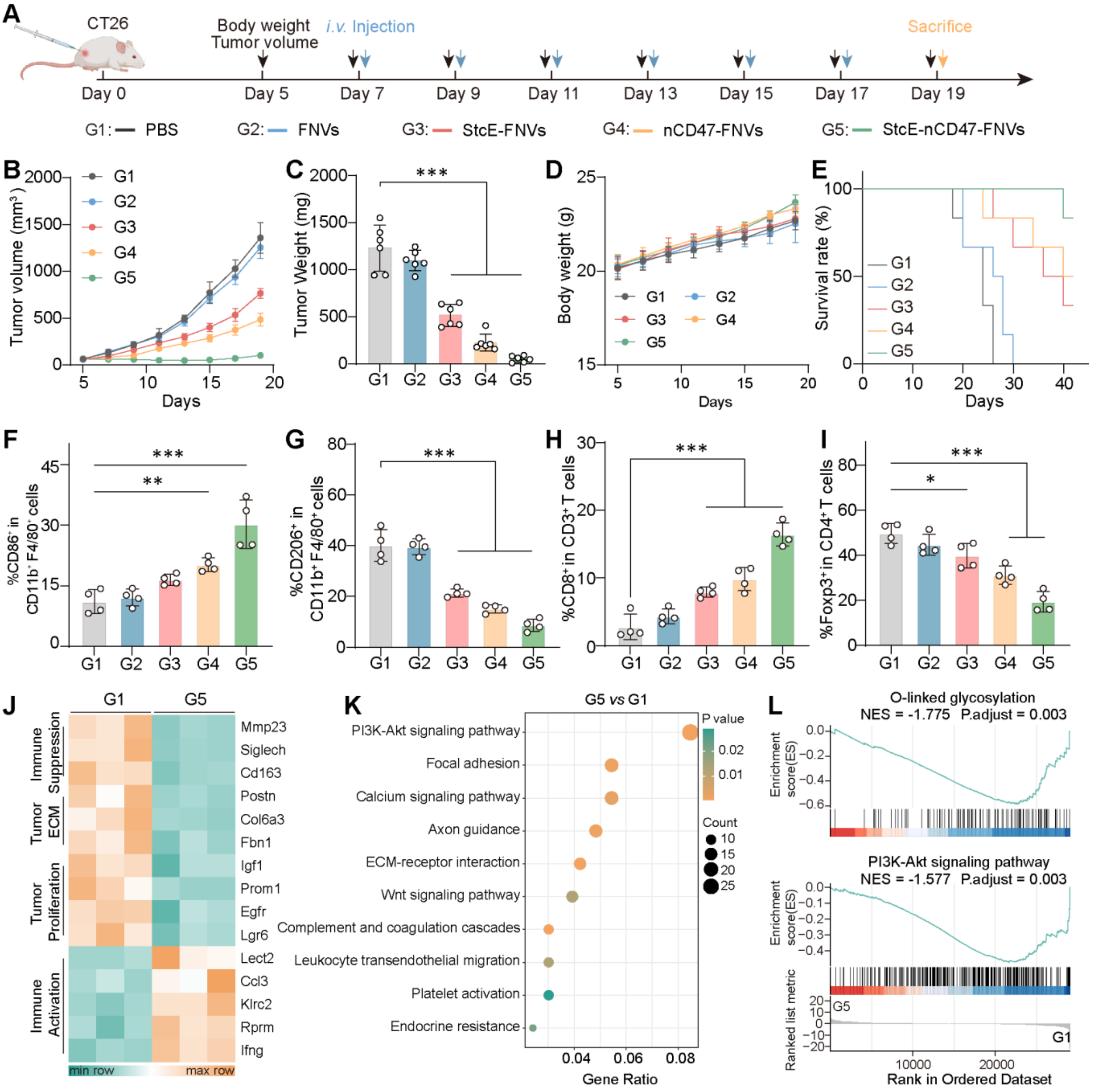

**Fig. 4. *In vivo* antitumor efficacy of different treatments in CT26 tumor-bearing mice.** (*A*) Schematic illustration of the experimental design and treatment schedule. CT26 tumor-bearing mice received six intravenous injections (blue arrows) of the indicated formulations beginning on day 7. Tumor volume and body weight were monitored (black arrows) until sacrifice on day 19. The five groups were: G1 (Blank), G2 (FNVs), G3 (StcE-FNVs), G4 (nCD47-FNVs), and G5 (StcE-nCD47-FNVs). (*B*) Tumor growth curves, (*C*) tumor weights at study endpoint, (*D*) body weight changes, and (*E*) survival curves. (*F-I*) Quantitative analysis of tumor-infiltrating immune cells, including (*F*) CD11b$^+$CD86$^+$ macrophages, (*G*) CD11b$^+$CD206$^+$ macrophages, (*H*) CD3$^+$CD8$^+$ T cells, and (*I*)

$CD4^+Foxp3^+$ T cells. (*J*) Heatmap of differentially expressed genes (DEGs, FDR-corrected $P < 0.05$) associated with immune suppression, immune activation, tumor proliferation, and extracellular matrix (ECM) in CT26 tumors from Blank and StcE-nCD47-FNVs-treated mice. (*K*) KEGG pathway enrichment analysis of DEGs between StcE-nCD47-FNVs-treated and Blank groups. (*L*) Gene Set Enrichment Analysis (GSEA) plots in StcE-nCD47-FNVs-treated tumors compared with Blank controls. Data are presented as mean ± S.D. (*B-E, n* = 6; *F-I, n* = 4; *J-L, n* = 3). $^{*}P < 0.05$, $^{**}P < 0.01$, $^{***}P < 0.001$. FNVs (HEK293T-NVs: CT26-NVs =1:3, no functional proteins), StcE-FNVs (HEK293T-StcE-NVs: CT26-NVs =1:3, glycocalyx hydrolysis only), nCD47-FNVs (HEK293T-NVs: CT26-nCD47-NVs =1:3, CD47 blockade only), StcE-nCD47-FNVs (HEK293T-StcE-NVs: CT26-nCD47-NVs =1:3, combination).

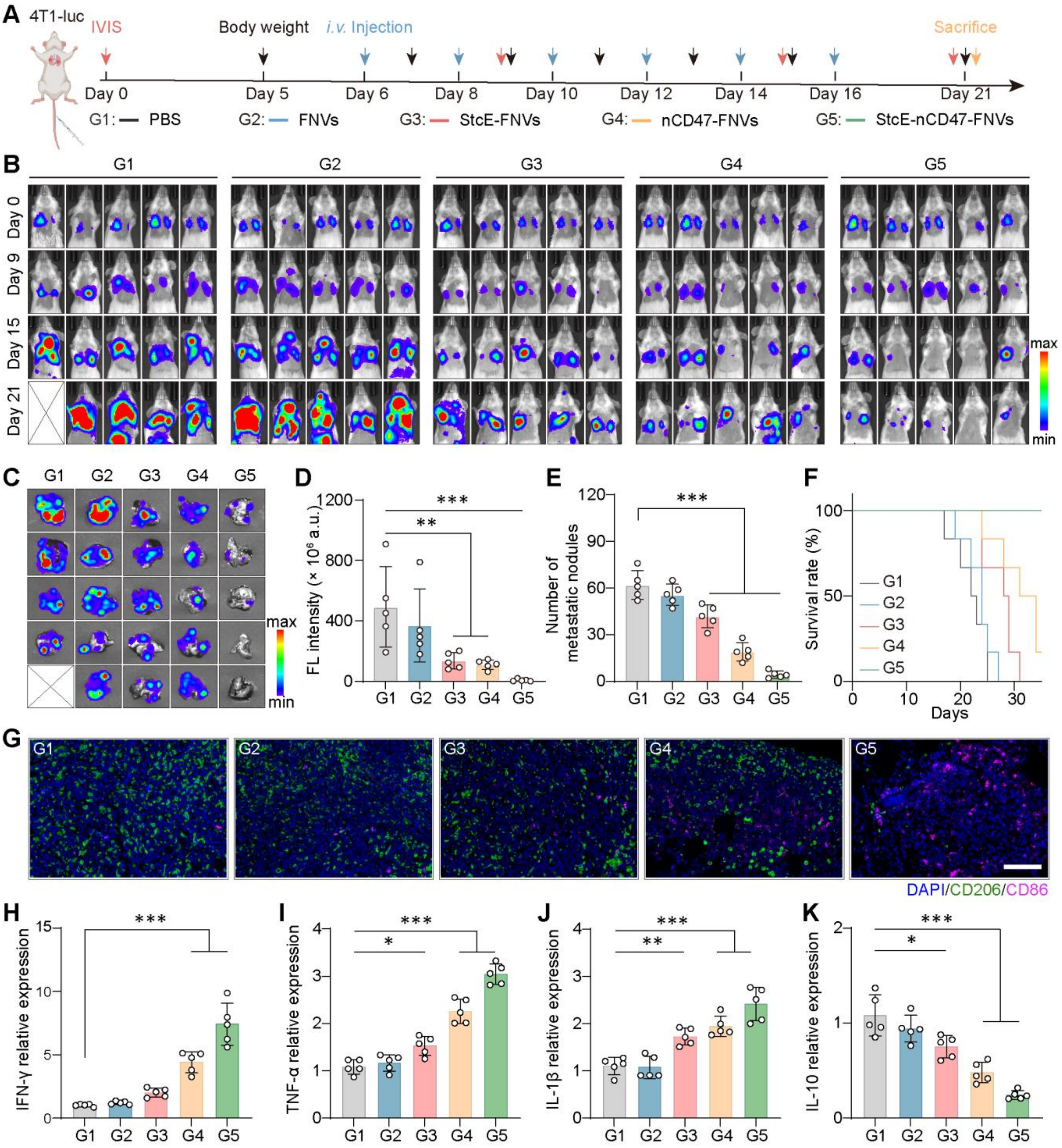

**Fig. 5. *In vivo* antitumor efficacy in a 4T1 lung metastasis model.** (*A*) Schematic illustration of the experimental design. The 4T1 lung metastasis model was established by intravenous injection of 4T1-luc cells. From day 6, mice received six doses of the indicated formulations every other day (blue arrows). Tumor burden was monitored by *in vivo* imaging system (IVIS, red arrows), and body weight was measured throughout (black arrows). The five groups were: G1 (Blank), G2 (FNVs), G3 (StcE-FNVs), G4 (nCD47-FNVs), and G5 (StcE-nCD47-FNVs). (*B*) Representative IVIS bioluminescence images of tumor-bearing mice on days 0, 9, 15, and 21, showing tumor progression. (*C*) *Ex vivo*

bioluminescence imaging of excised lungs at endpoint. (*D*) Quantification of lung bioluminescence intensity and (*E*) number of metastatic nodules. (*F*) Kaplan-Meier survival curves of mice receiving different treatments. (*G*) Immunostaining of macrophage infiltration in lung tumors across treatment groups. Scale bar, 100 μm. (*H*-*K*) RT-qPCR analysis of intratumoral cytokine mRNA expression levels, including pro-inflammatory cytokines (*H*) IFN-γ, (*I*) TNF-α, (*J*) IL-1β, and the anti-inflammatory cytokine (*K*) IL-10. Data are presented as mean ±S.D. ($n = 5$) *$P < 0.05$, **$P < 0.01$, ***$P < 0.001$. FNVs (HEK293T-NVs: 4T1-NVs =1:3, no functional proteins), StcE-FNVs (HEK293T-StcE-NVs: 4T1-NVs =1:3, glycocalyx hydrolysis only), nCD47-FNVs (HEK293T-NVs: 4T1-nCD47-NVs =1:3, CD47 blockade only), StcE-nCD47-FNVs (HEK293T-StcE-NVs: 4T1-nCD47-NVs =1:3, combination).